Magnetization mechanisms in ordered arrays of polycrystalline $Fe_{100-x}Co_x$ nanowires

M. S. Viqueira[1], N. Bajales[1], S. E. Urreta[2], P. G. Bercoff [1,2,†]

[1]Instituto de Física Enrique Gaviola – CONICET.

[2]Facultad de Matemática, Astronomía y Física, Universidad Nacional de Córdoba.

Ciudad Universitaria, 5000, Córdoba, Argentina.

[†] Corresponding author: P. G. Bercoff. Email: bercoff@famaf.unc.edu.ar

Abstract

Magnetization reversal processes and coercivity mechanisms in polycrystalline $Fe_{100-x}Co_x$ nanowire arrays, resulting from an AC electrodeposition process, are investigated. The array coercivity is described on the basis of polarization reversal mechanisms operating in individual wires, under the effect of inter-wire dipolar interactions described by a mean field approximation. For individual wires, a reversal mechanism involving the nucleation and further expansion of domain-wall like spin configuration is considered. The wires have a mean grain size larger than both the nanowire diameter and the exchange length, so localized and non cooperative nucleation modes are considered. As the Co content increases, the alloy saturation polarization gradually decreases, but the coercive field and the relative remanence of the arrays increase, indicating that they are not controlled by the shape anisotropy in all the composition range. The coercive field dependence on the angle between the applied field and the wire long axis is not well described by reversal mechanisms involving nucleation and further displacement of neither vortex nor transverse ideal domain walls. On the contrary, the angular dependence of the coercive field observed at room temperature is well predicted by a model considering nucleation of inverse domains by localized curling, in regions smaller than the grain size, exhibiting quite small aspect ratios as compared to those of the entire nanowire. In arrays with higher Co contents, a transition from an initial (small angle) localized curling nucleation mechanism to another one, involving localized coherent rotation is observed at about $\pi/4$.

PACS: 75.75.Cd Fabrication of magnetic nanostructures; 75.75.-c Magnetic properties of nanostructures; 75.30.Gw Magnetic anisotropy; 75.60.Jk Magnetization reversal mechanisms.

1. Introduction

Magnetization reversal mechanisms in ferromagnetic nanowires have been extensively investigated [1-10], and overviews of the results on wires embedded in the template they were grown in [11], are given in the reviews of Sellmyer *et al.* [12] and Vázquez *et al.* [13]. In single crystalline, uniform and short wires, with quite low aspect ratios, magnetization reversal mechanisms involving de-localized switching modes − like coherent rotation [14] and curling [7] − are considered, while localized magnetization reversal modes are predicted for long and wide single crystalline and also for polycrystalline nanowires [2-5, 12,13].

Isolated individual soft-magnetic nanowires exhibit square hysteresis loops [1], due to an abrupt magnetization reversal between the two possible remanent states. However, the hysteresis of a full array of such nanowires exhibits non-square loops as a result of size/shape anisotropy distributions in the sample and also due to magnetic dipolar interactions between nanowires [15-18]. In fact, the hysteresis loop shape results from the competition between the effective anisotropy field of individual wires and the dipolar interaction fields of the whole array. The dipolar coupling between wires may be described in a mean field approximation by an additional uniaxial anisotropy term favoring an in-plane easy axis [12,13,15]; for planar, regular arrays of magnetic nanowires this dipolar demagnetizing field is $\mu_0 H_{dip} = - c P J_S$, with J_S the saturation polarization, P the template porosity and c a constant. Then, by changing the nanowire packing density through P [15] the magnetization easy axis can be changed from an out-of-plane easy axis, parallel to the wire length, to an in-plane easy axis.

In long cylindrical and uniform structures, the magnetization mechanism is proposed to be controlled by the nucleation of a domain wall [2,12,13] which, depending on the radius and on the nanowire material, may be a vortex domain wall or a transverse wall; after nucleation these walls move at very high velocities along the wires. If the single crystalline wire is thin enough, the nucleation/propagation of a transverse wall results the preferred mode for magnetization reversal. These models involving localized nucleation and further expansion of a single, ideal domain wall

through the wires are rigorously valid for single crystalline wires and may be applied to individual grains in cases where the mean grain size is quite large as compared with the domain wall size and the wire diameter.

In polycrystalline nanowires, nucleation localization is caused by inhomogeneities [3,4]; grain boundaries, fluctuations in the wire thickness, atomic defects, grain misalignment and/or geometrical features at the wire ends lead to strong localization of the nucleation mode. Some authors suggest that the angular dependence of coercivity is consistent with a process controlled by coherent rotation or curling in a volume even smaller than the grain size d_G in the wire. For example, Wegrowe *et al.* [19] report for Ni nanowires, that the field and angular dependence of the magnetoresistance may only be quantitatively explained by the usual anisotropic magnetoresistance model, if the nucleation volume is assumed to be a "rugby ball" with a volume 50 times smaller than that of the whole wire, and with an aspect ratio $a_r^* \approx 2$ .This is a very small value considering that the Ni wires have $a_r = 100$. Quite small activation volumes are also found in magnetic viscosity measurements [12], indicating that thermally activated magnetization processes are controlled by the localized nucleation of an inverse domain surrounded by a wall-like spin configuration. Activation volume values of about $(11.5 \text{ nm})^3$, $(12.8 \text{ nm})^3$ and $(18 \text{ nm})^3$ are reported [12] for Fe (D=9 nm; d_G = 40 nm, L= 1μm), Co (D=20 nm; L= 1μm) and Ni (D=18 nm; d_G = 10 nm, L=1μm) nanowires respectively, at room temperature and at the coercive field. Then, in polycrystalline nanowires localized coherent rotation or localized curling should be considered as nucleation mechanisms.

Another aspect considered in magnetically hard polycrystalline nanowires, with a high anisotropy constant K_C ($K_C \gg M_0^2$), is the cooperative or non-cooperative nature of the nucleation mode [2]; when the exchange length in the material, l_{ex} ($= \sqrt{A/K_C}$, with A the exchange and K_C the magneto-crystalline anisotropy constants) is larger than the crystallite size d_G of the wire, a random anisotropy effect defines a nucleation localization length λ_{loc} which may involve more than a single grain. This *inter*-granular exchange interaction makes the nucleation mode cooperative.

In the case of magnetically semi-hard and soft polycrystalline nanowires, magnetostatic surface charges reduce the role of the polycrystalline anisotropy and K_C is often replaced by an effective anisotropy constant K_{eff} containing magneto-crystalline, shape and magneto-elastic contributions [12, 13]. A qualitative understanding of the nucleation localization phenomenon, governed by the sample polycrystalline nature, is described by Skomski *et al.* [2] in a mechanism map or phase diagram involving magnetic and structural characteristic lengths where different regimes are described.

Nucleation of a transverse or a vortex domain wall has been proposed to be the mechanism controlling the individual nanowire coercivity in many systems as Ni [9], Co [10, 13], CoNi [20], FeCo [21] and FeCoCu [22], but the predictions of these models for the angular dependence of the coercive field of ordered arrays of such nanowires, $\mu_0 H_C(\phi)$, are not quite satisfactory. In some cases, a correction for interwire dipolar interaction is proposed to improve the agreement with experimental data. In this sense, this dipolar contribution is reported to depend on the wire length. In FeCoNi nanowire arrays, Samanifar *et al.* [23] find, on the basis of first-order reversal curve (FORC) measurements, a linear correlation between the magnetostatic interactions and the nanowire length. With increasing length from 5 to 40 μm, the coercivity and squareness decrease by approximately 55% and 70%, due to the enhanced magnetostatic interactions. These interactions are characterized by a magnetic field H_{int} (=Hc^{FORC} - H_C^{Array}) with Hc^{Array} the mean value of the experimentally measured coercivity, and Hc^{FORC}, the mean coercive field of an individual nanowire. Positive values of H_{int} are obtained for nanowires longer than 15 μm while negative values (indicating a magnetizing overall effect) of about -50 Oe are obtained for wires 175nm in diameter and shorter than 5 μm ($a_r \lesssim 30$). These results indicate that this contribution may be important.

In this article we describe the magnetization reversal processes and the coercivity mechanisms in polycrystalline Fe$_{100-x}$Co$_x$ nanowire arrays, on the basis of polarization reversal mechanisms operating in individual wires under the effect of inter-wire dipolar interactions, described by a mean field approximation.

The mechanisms considered for local nucleation are curling or coherent rotation in a relatively small volume (nucleus), with a nearly prolate spheroid shape, and low aspect ratio as compared to the one of the entire wires. This nucleus may be smaller than the grain size in the wire or involve a few neighbor grains, leading to cooperative nucleation modes. In the present case, we consider samples with grain size larger than both the nanowire diameter and the exchange length to promote localized and non cooperative nucleation modes. All these assumptions lead to a better description of experimental data, in particular the orientation dependence of the coercive field, and the quite small activation volumes measured in viscosity experiments [12].

The changes observed in the coercive field and the relative remanence with the alloy composition indicate that in these polycrystalline nanowires, shape anisotropy is not predominant at low saturation polarization values (Co-rich wires). In fact, increasing the Co content has a hardening effect on coercivity and remanence, likely arising from competitive magnetocrystalline energy.

2. Experimental procedure

$Fe_{100-x}Co_x$ (x= 0, 29, 45, 68, 100) nanowire arrays were prepared by electrodepositing the metal ions within the pores of an anodized aluminum oxide (AAO) membrane [11]; these membranes, acting as hard templates, exhibit a hexagonal pore array of quite uniform diameter and length. Porous AAO templates were prepared, by the conventional two-step anodizing process of high purity (99.995%) aluminum foils in a 0.3 M oxalic acid solution at 276 K, with a DC voltage of 20 V. Prior to the anodization process the foils were degreased in an acetone bath and electropolished in a mixture of sulfuric and phosphoric acid.

In these conditions, pores with nominal diameter of 20 nm and about 1-2 μm in length were obtained. The template porosity P is estimated [24] as $P = (\pi/2\sqrt{3})(D/D_{int})^2$, with D the pore diameter and D_{int} the mean centre-to-centre interpore distance in the array. A mean value of $P = (0.11 \pm 0.01)$ is obtained, in good agreement with the ten%-porosity law [24].

The electrodeposition of $Fe_{100-x}Co_x$ nanowires with different compositions was carried out in an aqueous electrolytic bath containing Fe and Co ions, prepared with $CoSO_4$ $7H_2O$ 0.2M, $FeSO_4$ $7H_2O$ 0.2 M, 0.009 M ascorbic acid (to avoid iron oxidation), and HBO 0.5M, which was added to enhance conductivity. The pH value was adjusted to 5 by adding few drops of diluted H_2SO_4. The electrodeposition was conducted at room temperature under a sinusoidal wave of 200 Hz and 16 V_{rms}, during a few minutes; a two electrode electrochemical cell was used, where the aluminum still attached to the AAO template served as a working electrode and a graphite rod as an auxiliary one.

Sample morphology, composition and microstructure were investigated by scanning electron microscopy (SEM-STEM) in a FE-SEM Sigma Zeiss device with an Oxford EDS system (LAMARX), and by X-ray diffraction techniques in a Philips PW 3830 X-ray diffractometer with Cu Kα radiation (λ = 1.5418 Å), in the 2θ range between 30º and 90º, in the Bragg-Brentano configuration. Samples for XRD measurements were prepared by dissolving the remaining Al substrate in a $CuSO_4$ and HCl solution, while for SEM observation the nanowires were further liberated from the template by dissolving the alumina membrane with aqueous 1M Na(OH). When possible, the mean crystallite size of the nanowires was estimated using the Scherrer formula [25].

Magnetic properties were characterized by measuring the hysteresis loops at different relative orientations between the sample and the applied magnetic field: from ϕ=0º (PA, with the magnetic field parallel to the long nanowire axis) to ϕ=90º (PE, with the magnetic field perpendicular to the long nanowire axis). Room temperature magnetic hysteresis loops were performed in a Lakeshore 7300 vibrating sample magnetometer with a maximum field of 1.5 T.

The total magnetic moment of the assembly has contributions from the Al support (paramagnetic), the alumina template (diamagnetic) and the metallic wires filling the pores (ferromagnetic) but the ferromagnetic component is dominant.

3. Results and Discussion

3.1. Morphology and structure

Typical alumina templates (20±4) nm in diameter are shown in Figure 1.a (top view) and 1.b (side view); Figure 1.c provides a complete view of these nanowires, after both, the removal of the Al support and a partial dissolution of the alumina template. Based on similar images, the inter-pore distance, the pore wall thickness and the wire mean diameter and length were estimated for all samples, together with the mean aspect ratio (a_r) of the array, which reached values between 40 and 65 in all the cases.

It is found - see Table 1 - that the nanowire diameter is somewhat smaller than the pore diameter, as determined from SEM micrographs. The wire mean length is controlled by the electrodeposition time and values of (1.0±0.3) µm are obtained.

For each sample, the mean array composition corresponds to the average of ten EDS measurements taken on large nanowire colonies, after dissolving the remaining Al film and the alumina template.

X-ray diffraction patterns corresponding to arrays of different composition, measured after removal of the aluminum substrate, are shown in Figure 2. All the iron-containing samples have a *bcc* cubic structure with a preferred (110) orientation (intermediate between the hard (111) and the easy (100) ones) along the wires. The narrow peak at 31.66° corresponds to the polystyrene layer (JCPDS card no. 00-0130836) deposited onto the alumina membranes to improve their mechanical resistance. Based on the metallic Cobalt-Iron data (JCPDS card no. 00-048-1817 and JCPDS card no. 00-048-1818), the peaks at about 44°, 65° and 82° are indexed as the (110), the (200) and the (211) reflections of cubic *bcc* Fe-Co alloys. The pattern corresponding to the Co nanowire array is consistent with *hcp*-Co (JCPDS card no. 00-005-0727) and exhibits a marked (001) hexagonal texture.

The average crystallite size d_G of samples in Figure 2 are roughly estimated using the Scherrer equation [22]: $d_G = (0.9\ \lambda)/(B\ \cos\theta)$, with B (in radians) the peak intrinsic breadth after subtraction of the instrumental contribution, λ the X-ray wavelength and θ the Bragg angle. The resulting values, which correspond to a coherence length along the wire axis, are listed in Table 1. For samples $Fe_{71}Co_{29}$ and $Fe_{32}Co_{68}$ the grain size was also estimated, using SEM-STEM techniques −see Figure 3 and 4− leading to similar values, while those corresponding to pure Fe samples were determined by TEM (not shown).

Table 1. Mean grain size d_G, mean nanowire length L and diameter D corresponding to the different samples. Magnetic lengths as the coherence diameter $D_{coh,}(= 7.30\ \sqrt{\mu_0\ A/J_S^2}\ )$ [2] and the exchange length $L_{ex}\ (=\sqrt{\dfrac{2A\mu_0}{J_S^2}})$, estimated from parameters quoted in Table 2 are also included for comparison with the nanowires' dimensions.

Sample	d_G [nm]	L [µm]	D [nm]	D_{coh} [nm]	L_{ex} [nm]
Fe	100±20	0.8±0.1	20±2	14.6	2.0
$Fe_{71}Co_{29}$	25±5	1±0.1	20±2	12.4	1.7
$Fe_{55}Co_{45}$	30±5	0.8±0.1	20±2	12.6	1.7
$Fe_{32}Co_{68}$	38±5	1.3±0.2	20±2	14.6	2.0
Co	42±10	0.8±0.1	18 ±2	17.4	2.3

The electrodeposited nanowires are polycrystalline, with mean grain size values larger than the wire diameter, so "bamboo-like" grain structures cannot be excluded, especially in Fe100 samples. From these results, a reduction in grain size with the iron content cannot be rigorously stated because of large determination errors, but it is known that increasing the Fe(II) content in the solution changes the cobalt deposition mechanism. In fact, it has been reported [26] that Fe(II) inhibits the nucleation and early growth of Co while the presence of Co(II) strongly catalyzes iron deposition.

3.2. *Room temperature magnetic properties*

Room temperature hysteresis loops of the arrays, measured with the applied magnetic field forming two different angles ϕ with the wire major axis, are shown in Figure 4 for three nanowire arrays with similar nominal wire diameter and different compositions. The saturating field, the coercive field and the remanent magnetic moment measured in the PA configuration are larger, indicating that this is an easy magnetization direction in the array, that is, there is an easy magnetization axis perpendicular to (out of plane) the Al substrate foil and parallel to the nanowire length. Values of the coercive field and the relative remanent polarization for the PA configuration are listed in Table 2.

Table 2. Room temperature values of magnetic parameters. Coercive field $\mu_0 H_C$ and relative remanence or loop squareness S ($=J_R/J_S$), with J_R the remanent and J_S the saturation polarization, respectively. These values correspond to measurements performed with the applied magnetic field parallel to the wire length (PA configuration). Values of the saturation polarization J_S and the crystalline anisotropy energy K_C for different compositions, taken from reference [27] are also quoted.

Sample	$\mu_0 H_C$ [T]	S	J_S [T]	$K_C \times 10^5$ [Jm^{-3}]
Fe	0.2110	0.74	2.16	0.48
$Fe_{71}Co_{29}$	0.1785	0.74	2.54	0.38
$Fe_{55}Co_{45}$	0.2370	0.82	2.50	-0.07
$Fe_{32}Co_{68}$	0.2405	0.92	2.17	-0.38
	0.1735	0.65	1.82	5
Co *hcp*				
fcc				0.62

A non monotonic dependence of the coercive field on the Co content is found, as illustrated in Figure 5, in agreement with data previously reported in [16]. However, it is worth noting that in the three *bcc* Co-Fe alloyed samples, the coercive field and the squareness S both increase with the Co content, while the saturation polarization (determining the shape anisotropy) and the crystalline anisotropy decrease [27]. Bran *et al*. [22] attribute a similar behavior observed in $Fe_{28}Co_{67}Cu_5$ nanowire arrays, 8 µm long and 18 -27 nm diameter, to a change in the coercivity mechanism, from vortex to transverse domain-wall reversal modes as the saturation polarization decreases. As coercivity for the transverse wall reversal mode is always larger than that for the vortex wall mode, a reduction in J_S may lead to a larger coercivity. Considering these ideas we propose that a transition occurs from a regime where the spin configuration minimizes the magnetostatic energy (vortex like) to another one, at lower saturation polarization values, where configurations become more uniform to minimize exchange and magnetocrystalline energies.

The wire diameter in all the samples satisfies $D \geq D_{coh} = 7.30 \sqrt{\mu_0 A/J_S^2}$, so localized magnetization reversal modes are favorable. Moreover, due to imperfections, localized reversal modes are predicted [3] even for wire diameters smaller than the coherence diameter. Regarding

dipolar interactions both, P and the wire diameter D are kept nearly constant, so only compositional changes must be considered to evaluate changes in these long range interactions between nanowires in the array.

3.3. *Magnetization mechanism*

Regarding the magnetization mechanisms, the chain-of-spheres model [6,16] assumes that no exchange interactions take place between the units in the chain, and that each grain reverses homogeneously, conditions that are not completely fulfilled in our case, where the grains are closely inter-related and in some cases their sizes are large enough to bear a magnetic domain wall-like spin configuration.

The localized nucleation modes and the small activation volumes measured in polycrystalline nanowires indicate that *local* microstructure features and *local* internal fields are important. In fact, when the reversal process is controlled by nucleation in a small volume, local magnetic properties and defects play a crucial role.

Nucleation processes were investigated by measuring the angular dependence of both, the coercive field and the relative remanent polarization as functions of the angle ϕ between the applied field and the nanowire major axis.

When polarization reversal initiates by the formation of a local inverse nucleus by a coherent rotation mechanism, the switching field $\mu_0 H_S^C$ for an individual and isolated nanowire as a function of ϕ may be expressed as [14,28]:

$$\mu_0 H_S^C(\phi) = \mu_0 \frac{2\,K_{eff}}{J_S} \frac{1}{(\cos\phi^{\frac{2}{3}} + \sin\phi^{\frac{2}{3}})^{\frac{3}{2}}} \tag{1}$$

with

$$K_{eff} = \alpha\,K_C + \beta\,\frac{(N_\parallel - N_\perp)}{\mu_0}\,J_S^2\,, \tag{2}$$

an effective anisotropy energy with magnetocrystalline and magnetostatic contributions. The first term depends on the crystalline texture, the domain wall width relative to the grain size (random anisotropy regime) and on structure defects, while the second one scales with the nanowire aspect ratio. Parameters α and β account for the reduced crystalline anisotropy and the reduced (magnetostatic) shape anisotropy, respectively, in the nucleation site; $N_\parallel$ and $N_\perp$ are the wire demagnetizing factors parallel and perpendicular to the wire long axis, respectively, with $(N_\parallel + 2\,N_\perp) = 1$. Assuming that the effect of the other wires in the array on each individual wire may be roughly approximated by a constant (no angular dependence) demagnetizating mean field given by $\mu_0 H_{dip} = -N_{eff}^C J_S$ with $N_{eff}^C = c\,P$ [15], the switching field of the array may be approximated by:

$$\mu_0 H_S^C(\phi) = \mu_0 \frac{2\,K_{eff}}{J_S} \frac{1}{(\cos\phi^{\frac{2}{3}} + \sin\phi^{\frac{2}{3}})^{\frac{3}{2}}} - N_{eff}^C J_S. \tag{3.a}$$

and the coercive field becomes [14]:

$$\mu_0 H_C^C(\phi) = \begin{cases} \left|\mu_0 H_S^C(\phi)\right| & 0 \le \phi \le \frac{\pi}{4} \\ 2\left|\mu_0 H_S^C\left(\frac{\pi}{4}\right)\right| - \left|\mu_0 H_S^C(\phi)\right| & \frac{\pi}{4} \le \phi \le \frac{\pi}{2} \end{cases} \tag{3.b}$$

Equations (3.a) and (3.b) have the general form proposed by H. Kronmüller [29] and D. Givord [30] for the coercivity of hard granular magnets. In the present case, shape effects associated to the wire aspect ratio are considered as a contribution to the effective uniaxial anisotropy, while the dipolar interaction between wires in the ensemble is considered trough an effective demagnetizing field applied to each nanowire.

When the inverse domain nucleates by a process of local curling, the nucleation field for an isolated wire –may be described considering reversal in a small prolate spheroid (nucleus) with an effective anisotropy K_{eff} given as before by contributions of crystalline and shape (related to the wire aspect ratio) anisotropies; following Aharoni [7,28,31]:

$$\mu_0 H_n^V = -\mu_0 \frac{2 K_{eff}}{J_s} + N_{eff}^V J_S \qquad (4)$$

with K_{eff} given by Eqn. 2 and $N_{eff}^V = \frac{k}{2}\left(\frac{D_{coh}}{D}\right)^2 + c P$ and $k = 1.2049$ [32]. The angular dependence of the nucleation field for a curling mechanism in an isolated prolate spheroid was also determined by Aharoni [7]; when the coercive field is controlled by the formation of an inverse nucleus by curling, the angular dependence of this field may be expressed, ignoring as before the angular dependence of the dipolar field, as [7]:

$$\mu_0 H_C^V(\phi) = \mu_0 \frac{2 K_{eff}}{J_s} \frac{\left(\varepsilon_\parallel N_\parallel - \frac{k L_x^2}{R^2}\right)\left(\varepsilon_\perp N_\perp - \frac{k L_x^2}{R^2}\right)}{\sqrt{\left(\varepsilon_\parallel N_\parallel - \frac{q^2 L_x^2}{R^2}\right)^2 \sin^2\phi + \left(\varepsilon_\perp N_\perp - \frac{q^2 L_x^2}{R^2}\right)^2 \cos^2\phi}} - N_{eff}^V J_S \qquad (5)$$

Here, $R = \frac{D}{2}$, is the mean wire radius and $L_x = \sqrt{\frac{2A\mu_0}{J_S^2}}$ is the exchange length, which is composition sensitive through J_S values, A is the exchange energy constant and K_{eff} is the effective uniaxial anisotropy previously defined in eqn (2). $\varepsilon_\parallel$ and $\varepsilon_\perp$ are factors adjusting the nucleus' effective demagnetizing factors, related to the local magnetostatic energy where the nucleus forms.
Equation (5) assumes that the effect of the nanowire geometry is to add a magnetostatic, shape dependent contribution to the uniaxial anisotropy at the nucleation site, but the angular dependence of coercivity is related to the nucleus aspect ratio. Again, the second term in the right hand of this equation is a mean value of the dipolar interaction field for applied fields forming angles between 0 and $\pi/2$ with the major wire axis.

Figures 6 a-e illustrate the experimental data for the orientation dependence of the coercive field in the investigated nanowire arrays; the solid lines correspond to the behaviors predicted by eqns. (3) or (5), depending on the wire nanostructure and composition. The parameters resulting from the best fit to the data are listed in Table 3.

These values should be taken as approximate and only indicative of different aspects of the magnetization reversal mechanism, as magnitudes depending on the applied field orientation are assumed as constants and the nucleus shape is considered to be a prolate spheroid. Nevertheless, the hypotheses of a small, spheroidal nucleus, independent of the actual nanowire geometry, and an enhanced uniaxial anisotropy scaling the wire aspect ratio provide a better fit to experimental curves in Figure 6, with physically reasonable parameters.

It is found that the arrays $Fe_{100-x}Co_x$ exhibit negative effective demagnetizing factors $N_{eff}^{V,C}$ suggesting that dipolar interactions between wires in the ensemble tend to stabilize magnetization, increasing the coercive force. As commented before, a similar behavior has been recently reported by Samanifar *et al.* [23] for short (L< 15 μm) $Fe_{47}Co_{38}Ni_{15}$ nanowire arrays. In this system, magnetizing fields of about 5 mT are measured when the coercive field of individual wires is near 30 mT and the saturation polarization is about 2 T. On the contrary, this factor is positive in Fe and Co wires leading to a demagnetizing dipolar field. The values observed are compatible with the array porosity $P = 0.11$.

In bulky pieces of Fe-Co alloys [27], the magnetocrystalline anisotropy value gradually decreases as the Fe content reduces, becoming negative below the equiatomic composition, in agreement with the values observed in the present work for the effective uniaxial anisotropy K_{eff} ; however, the values obtained are almost one order of magnitude larger than the K_C bulk values, confirming that another contribution to K_{eff} is present. In this sense, the fitted values are smaller but comparable to those of the shape anisotropy K_{sh} associated to a thin, long (infinite) cylinder, as shown in Table 3.

The resulting values for $\varepsilon_\parallel$ and $\varepsilon_\perp$, correcting the nanowire demagnetizing factors to obtain those of the small nucleus, are estimated assuming that this nucleus is a prolate spheroid; this may be not necessarily true, as suggested by the fact that $(\varepsilon_\parallel N_\parallel + 2 \varepsilon_\perp N_\perp) = 0.9 \mp 0.2$ in most of the samples, except in sample $Fe_{32}Co_{68}$, where a value of 0.5 is obtained. This later sample exhibits a transition in the nucleation mechanism, from curling (V) for $0 \leq \phi \leq \frac{\pi}{4}$ to coherent rotation (SW) for $\frac{\pi}{4} < \phi \leq \frac{\pi}{2}$, so the values of parameters $\varepsilon_\parallel$ and $\varepsilon_\perp$ are estimated with larger errors. In spite of these facts, if a prolate spheroidal shape is assumed, an apparent nucleus aspect ratio may be estimated [32,33], and values between 2-4 result, as suggested by Pignard *et al.* [34] for Ni nanowires. In the size range of our arrays the nuclear aspect ratio values could not be correlated with composition nor with the wire length or grain size.

Analytical models described here consider relatively homogeneous cylinders with the anisotropy axis coincident with the sample axis; instead, real wires are not homogeneous but a granular structure, often highly textured, leading to more than one anisotropy axis affecting the angular-dependence of the relative remanence and the coercive field.

The transition found in sample $Fe_{32}Co_{68}$ from a curling (V) to a coherent rotation (SW) nucleation mechanism near $\phi=\pi/4$ is consistent with a transition to a more uniform spin configuration in the nucleus as the crystalline become competitive to define K_{eff}.

Following Skomski *et al.*[2] all the samples in the present work are localized in Region II ($\delta w < d_G$ and $D < d_G$) corresponding to a non-cooperative nucleation mode. Then, the polarization reversal process in Fe-Co nanowires, may be described, as proposed by Givord *et al.* [30], considering successive stages. The first stage begins in a grain with the nucleation (by rotation or curling) of a domain of inverse magnetization in a defect, the second one with the passage of the domain wall from the defect to the principal phase and finally the domain wall traverses the whole grain. The first reversed grains may act as catalysts for reversion in the neighbor grains, promoting an avalanche effect along the nanowire. This cascade seems not too different from a domain wall like spin configuration travelling long distances along the wire.

Table 3. Values of the longitudinal and transversal demagnetizing factors $N_\parallel$ and $N_\perp$ [35] for individual nanowires, parameters ε, $N_{eff}^{V,C}$, $K_{sh} \left(= \frac{1}{2\mu_0}(N_\perp - N_\parallel) J_S^2 \right)$ and the effective crystalline anisotropy energy K_{eff} for different compositions. Labels SW and V indicate that equations (5) and (8) have been fitted, respectively.

Sample		$K_{eff}\ 10^5$ [Jm^{-3}]	$K_{sh}\ 10^5$ [Jm^{-3}]	$N_{eff}^{V,C}$	$N_\parallel$	$N_\perp$	$\varepsilon_\parallel$	$\varepsilon_\perp$
Fe	V	8	9	0.07	0.0105	0.4947	40	0.5
$Fe_{71}Co_{29}$	V	5.5	12.5	-0.10	0.0084	0.4958	15	0.7
$Fe_{55}Co_{45}$†	V	-5	12	-0.02	0.0105	0.4947	12	0.9
	V	2		0.12	0.0105	0.4947	33	0.4
$Fe_{32}Co_{68}$†	V	-6	9	-0.07	0.0065	0.4967	47	0.2
	SW	-4		-0.20			-	-
Co	V	-5	6	0.01	0.0105	0.4947	35	0.3

† Curve fitted considering different functions for low ($\theta<\pi/4$) and high ($\theta\geq\pi/4$) angles, respectively.

4. Conclusions

The magnetization reversal mechanisms operating in $Fe_{100-x}Co_x$ (x = 0, 29, 45, 68 and 100) nanowires, packed in a regular hexagonal array (provided by a self-assembled alumina template) are described. The wires are (1 ± 0.2) µm long, (20 ± 2) nm diameter, with grains larger than the wire diameter.

The effective magnetic anisotropy describing coercivity is found to be controlled by the shape anisotropy in samples with large Fe content, but the values obtained are lower than those corresponding to the entire wire, mainly due to the polycrystalline nature of these wires. In *bcc* Co-Fe alloyed samples, coercive field and squareness *S* both increase with the Co content, while saturation polarization (which determines the shape anisotropy) decreases; this evidences that the effective anisotropy is not controlled by shape anisotropy in the whole composition range.

The reversal is assumed to initiate by a local nucleation event. The coercive field in a given array is modeled considering the critical field for polarization reversal in an individual wire, affected by a mean dipolar field provided by the other wires in the array.

The room temperature dependence of the coercive field on the angle between the applied field and the major wire axis' direction is consistent with two localized nucleation modes; demagnetization may initiate by curling or coherent rotation in a small prolate spheroid volume (nucleus), with low apparent aspect ratios (2-4) as compared with the aspect ratio of the entire wire. This model leads to a much better description of the orientation dependence of the array coercive field.

It is found that nucleation by local curling explains all data for values of ϕ below $\pi/4$; for the alloy with the largest Co content two regimes are found, with nucleation by local curling at low angles and by coherent rotation above about $\pi/4$.

References

1. R. Hertel, Computational micromagnetism of magnetization processes in nickel nanowires, *J. Magn. Magn. Mater.* **249** (1–2), 251–256 (2002).

2. R. Skomski, H. Zeng, M. Zheng, D. J. Sellmyer, Magnetic localization in transition-metal nanowires, *Phys. Rev.* B **62** (6) , 3900-3904 (2000).

3. R. Skomski, Zeng, H., Sellmyer, D.J., Incoherent magnetization reversal in nanowires, *J. Magn. Magn. Mater.* **249**, 175–180 (2002).

4. G. C. Han, B. Y. Zong, P. Luo, Y. H. Wu, Angular dependence of the coercivity and remanence of ferromagnetic nanowire arrays, *J. of Appl. Phys.* **93** 11 1, 9202-9207 (2003).

5. R Skomski, Exact nucleation modes in arrays of magnetic particles**,** *J. Appl. Phys.* **91** (10) , 15 (2002).

6. I. S. Jacobs, C. P. Bean, An Approach to Elongated Fine-Particle Magnets, *Phys. Rev.* **100** (4), 1060-1067 (1955).

7. A. Aharoni, Angular dependence of nucleation by curling in a prolate spheroid, *J. Appl. Phys.* **82**, 1281 (1997).

8. P. Landeros, S. Allende, J. Escrig, E. Salcedo, D. Altbir, E. E. Vogel, Reversal modes in magnetic nanotubes, *Appl. Phys. Lett.* **90**, 102501 (2007).

9. R. Lavín, J. C. Denardin, J. Escrig, D. Altbir, A. Cortés, H. Gómez, Angular dependence of magnetic properties in Ni nanowire arrays, *J. Appl. Phys.* **106**, 103903 (2009).

10. R. Lavín, J. C. Denardin, A. P. Espejo, A. Cortés, H. Gómez,, Magnetic properties of arrays of nanowires: Anisotropy, interactions, and reversal modes, *J. Appl. Phys.* **107**, 09B504 (2010).

11. H. Masuda, K. S. Fukuda, Ordered Metal Nanohole Arrays Made by a Two-Step Replication of Honeycomb Structures of Anodic Alumina, *Science* **268**, 1466-1468 (1995).

12. D. J. Sellmyer, M. Zheng, and R. Skomski, Magnetism of Fe, Co and Ni nanowires in self-assembled arrays, *J. Phys.: Condens. Matter* **13** R433, 73 (2001).

13. M. Vazquez and L. G. Vivas. Magnetization reversal in Co-base nanowire arrays. *Phys. Status Solidi* B **248** 10, 2368–2381 (2011).

14. E. C. Stoner and E. P. Wohlfarth, A mechanism of magnetic hysteresis in heterogeneous alloys, *Philos. Trans. R. Soc. London* A **240** 599, 18 (1948).

15. A. Encinas-Oropesa, M. Demand, L. Piraux, I. Huynen, U. Ebels, Dipolar interactions in arrays of nickel nanowires studied by ferromagnetic resonance, *Phys. Rev.* B **63** 104415 (2001).

16. Zhan, Qing-Feng, Gao, Jian-Hua, Liang, Ya-Qiong, Di, Na-Li, Cheng, Zhao-Hua, Dipolar interactions in arrays of iron nanowires studied by Mössbauer spectroscopy, *Phys. Rev.* B **72,** 024428 (2005).

17. F. Zighem, T. Maurer, F. Ott, G. Chaboussant, Dipolar interactions in arrays of ferromagnetic nanowires: A micromagnetic study, *J. Appl. Phys.* **109,** 013910 (2011).

18. O. Dmytriiev, U. A. S. Al-Jarah, P. Gangmei, V. V. Kruglyak, R. J. Hicken, B. K., Mahato, B. Rana, M. Agrawal, A. Barman, M. M´at´efi-Tempfli, L. Piraux' S. M´at´efi-Tempfli, Static and dynamic magnetic properties of densely packed magnetic nanowire arrays. *Phys. Rev. B* **87,** 174429 (2013).

19. J-E. Wegrowe, D. Kelly, A. Franck, S. E. Gilbert, and J.-Ph. Ansermet, Magnetoresistance of Ferromagnetic Nanowires, *Phys. Rev. Lett.* **82** 18, 3681-3684 (1999).

20. L. G. Vivas, M. Vazquez, J. Escrig, S. Allende, D. Altbir, D. C. Leitao, and J. P. Araujo, Magnetic anisotropy in CoNi nanowire arrays: Analytical calculations and experiments*, Phys. Rev. B* **85**, 035439 (2012).

21. C. Bran , Yu. P. Ivanov , D. G. Trabada , J. Tomkowicz , R. P. del Real , O. Chubykalo-Fesenko, M. Vazquez, Structural Dependence of Magnetic Properties in Co-Based Nanowires: Experiments and Micromagnetic Simulations, IEEE Trans. on magnetics, 49, (8) 4491-4497 (2013).

22. C. Bran, Yu. P. Ivanov, J. García, R. P. del Real, V. M. Prida, O. Chubykalo-Fesenko, and M. Vazquez, Tuning the magnetization reversal process of FeCoCu nanowire arrays by thermal annealing, J. of Appl. Phys. 114, 043908 (2013).

23. S. Samanifar, M. Almasi Kashi, A. Ramazani, M. Alikhani Reversal modes in FeCoNi nanowire arrays:Correlation between magnetostatic interactions and nanowires length, J. of Magn. and Magn. Mater. 378 73–83 (2015).

24. K. Nielsch, J. Choi, K. Schwirn, R. B. Wehrspohn, and U. Gösele, Self-ordering Regimes of Porous Alumina: The 10% Porosity Rule, *Nano Lett*. **2,** 677 (2002).

25. A. L. Patterson, The Scherrer Formula for X-Ray particle size determination, *Phys. Rev.* **56**, 15 (1939).

26. R. Bertazzoli, D. Pletcher, Studies of the mechanism for the electrodeposition of Fe-Co alloys, *Electrochimica Acta* **38** (5), 616 (1993).

27. R. C. O'Handley, *Modern Magnetic Materials. Principles and Applications* (John Wiley and Sons. New York 2000).

28. A. Aharoni, Perfect and imperfect particles, *IEEE Tran. on Mag.* MAG-22 5, 478-483 (1986).

29. H. Kronmüller, K. D. Durst and M. Sagawa Analysis of the *magnetic* hardening mechanism in RE-FeB permanent magnets, *J. Magn. Magn. Mater.* **74,** 291 (1988).

30. D. Givord, M.E Rossignol and D.W. Taylor, Coercivity mechanisms in hard magnetic materials, *J. de Physique IV, Colloque C3, Suppl. J. de Physique* **111** 2, 95-104 (1992).

31. L. G. Vivas, M. Vazquez, J. Escrig, S. Allende, D. Altbir, D. C. Leitao, and J. P. Araujo, Magnetic anisotropy in CoNi nanowire arrays: Analytical calculations and experiments*, Phys. Rev. B* **85**, 035439 (2012).

32. A. Aharoni and S. Shtrikman, Magnetization Curve of the Infinite Cylinder, *Phys. Rev.* **109**, 1522-1528 (1958).

33. J. A. Osborn, Demagnetizing factors of the general ellipsoid. *Phys. Rev.* **67** (11), 351-357 (1945).

34. S. Pignard, G. Goglio, A. Radulescu, L. Piraux, S. Dubois, A. Decl´emy, and J. L. Duvail, Study of the magnetization reversal in individual nickel nanowires, *J. Appl. Phys.* **87**, 824 (2000).

35. P. Landeros, J. Escrig, and D. Altbir, D. Laroze, J. d'Albuquerque e Castro, P. Vargas, Scaling relations for magnetic nanoparticles, *Phys. Rev.* B **71**, 094435 (2005).
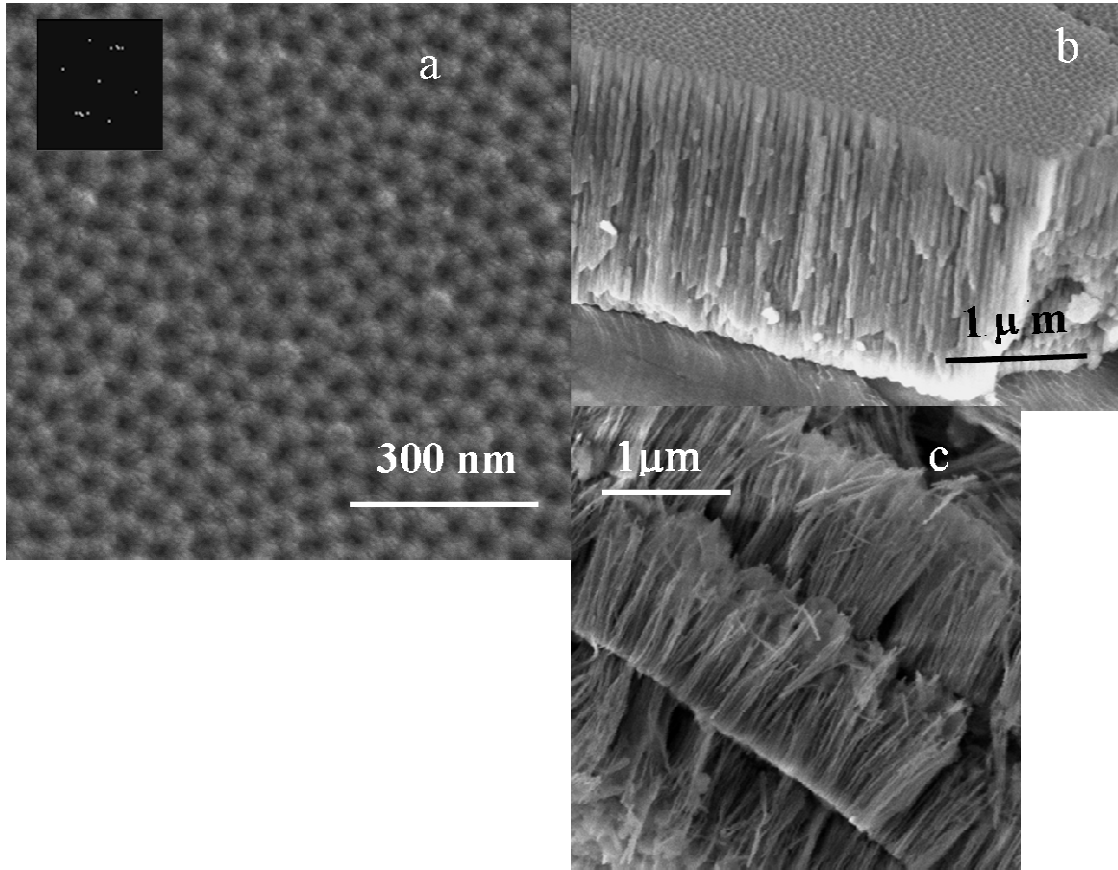
Figure 1. SEM micrographs showing a top view (a) and a side view (b) of an alumina template of 20 nm pore diameter. $Fe_{32}Co_{68}$ nanowires are shown in (c), after the partial dissolution of the alumina template.
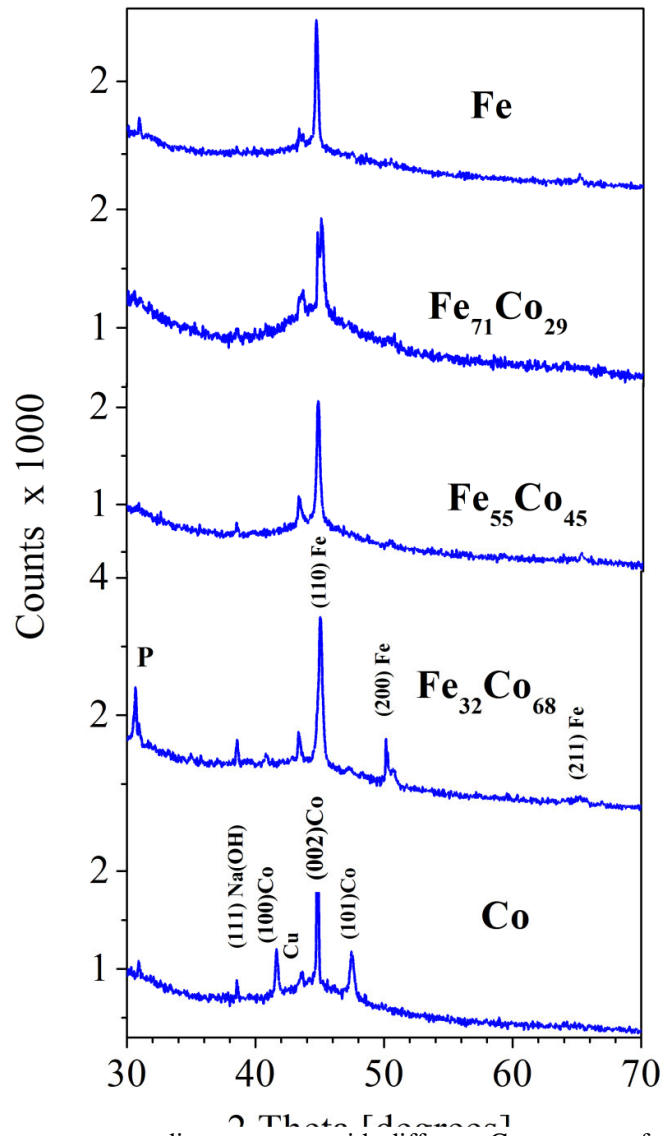
Figure 2. XRD patterns corresponding to arrays with different Co content, after removal of the Al substrate. The reflection denoted by P arises from the polystyrene layer added to improve the membrane mechanical resistance. Small Cu crystals, originated in the Al dissolution process are also detected.
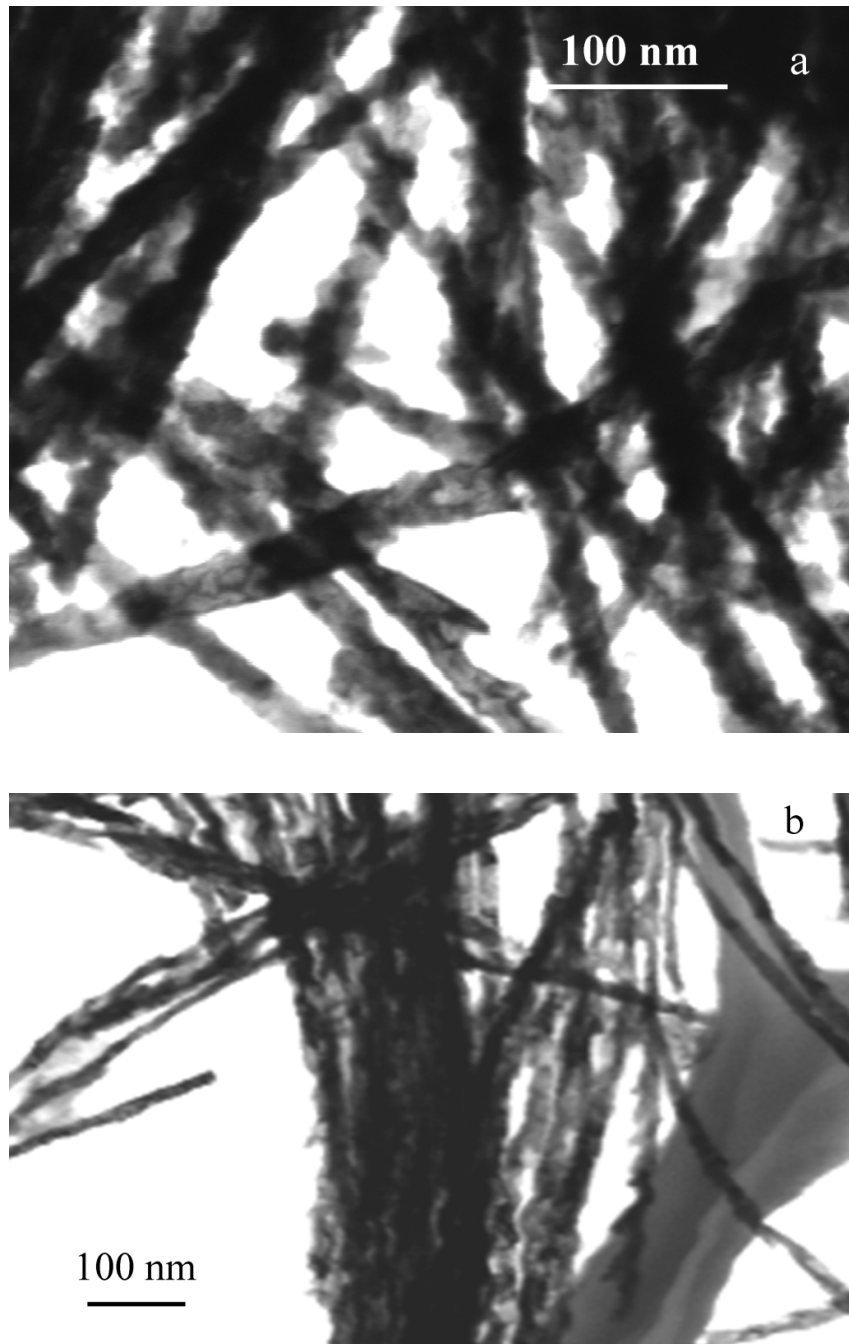
Figure 3. SEM-STEM micrographs of $Fe_{71}Co_{29}$ (a) and $Fe_{32}Co_{68}$ (b) nanowires. They are polycrystalline, with grain size reducing with the Co aggregate.
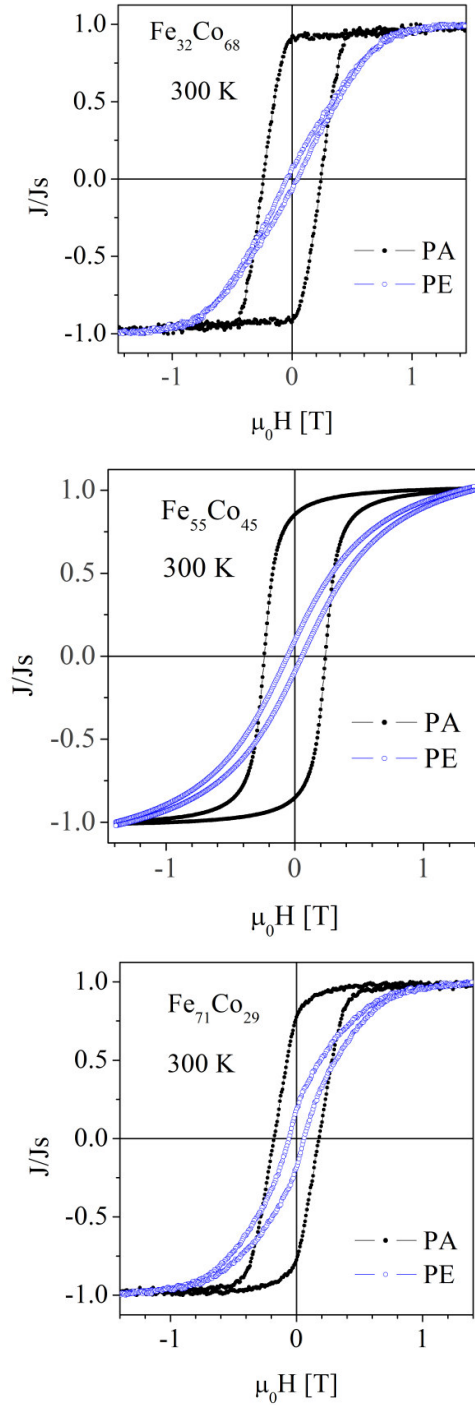
Figure 4. Room temperature hysteresis loops of samples $Fe_{100-x}Co_x$ measured with the applied field parallel (PA) and perpendicular (PE) to the nanowire major axis. The different loops obtained in these two configurations are consistent with a relatively large shape anisotropy.
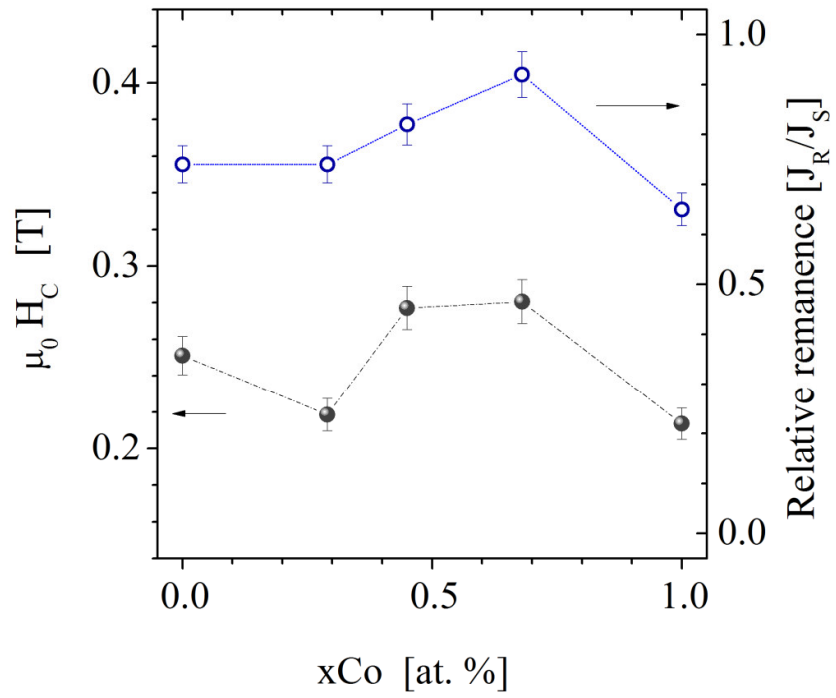
Figure 5. Room temperature coercive field as a function of the Co content, in arrays of 20 nm diameter nanowires.
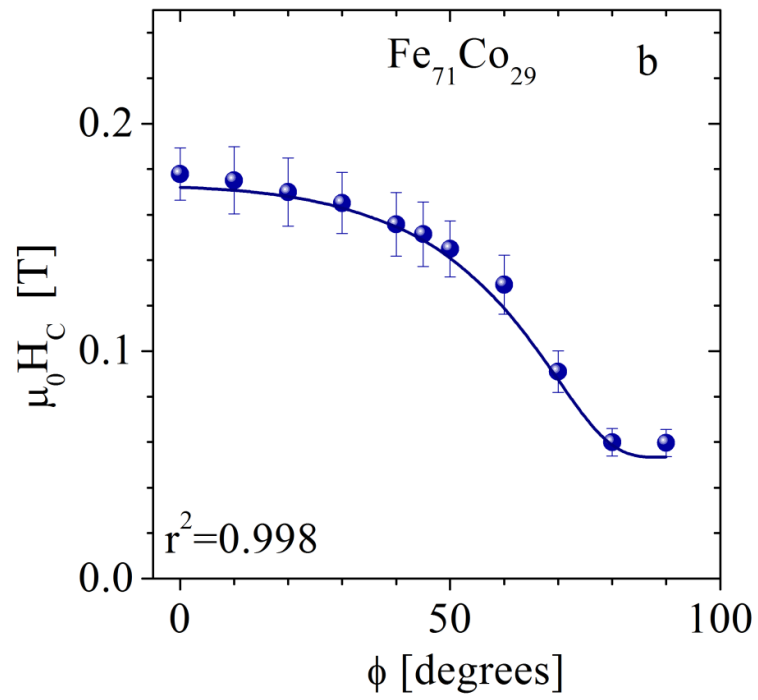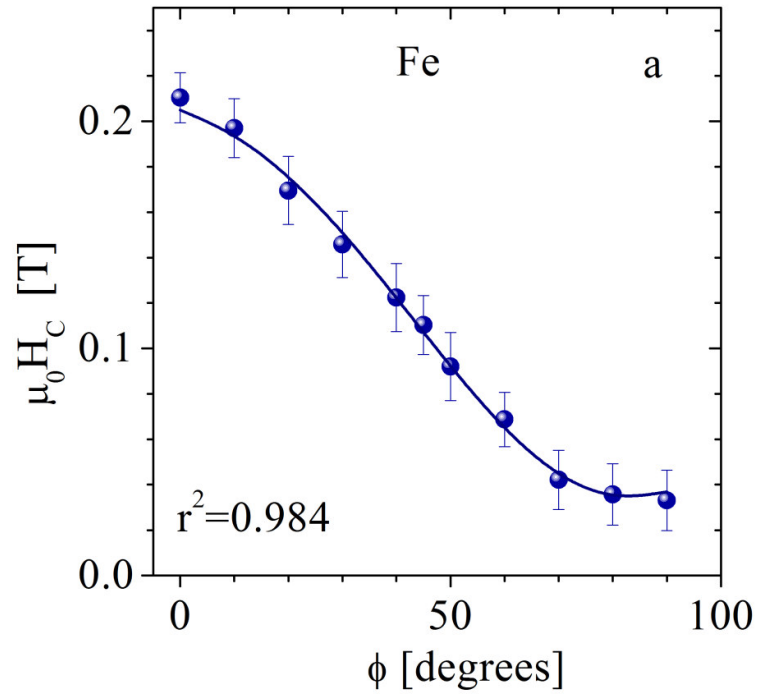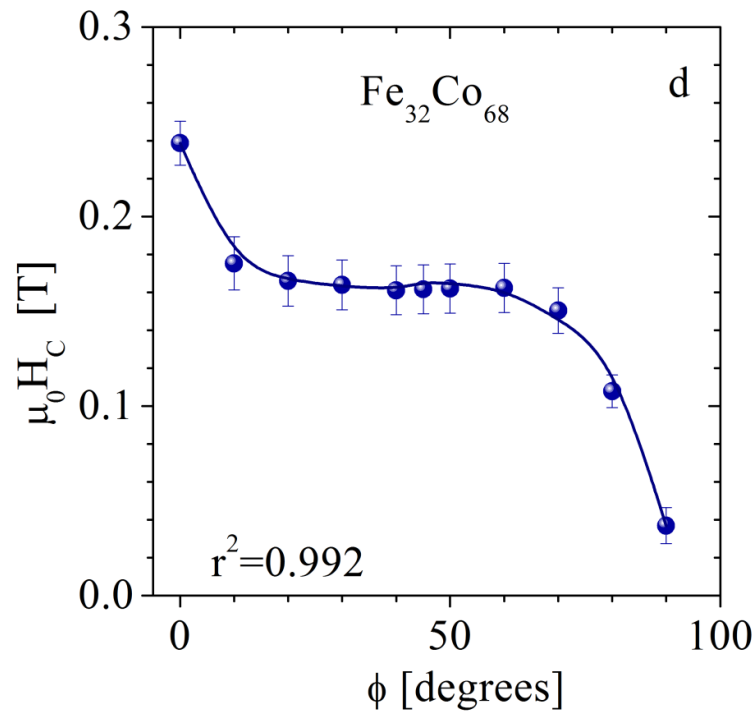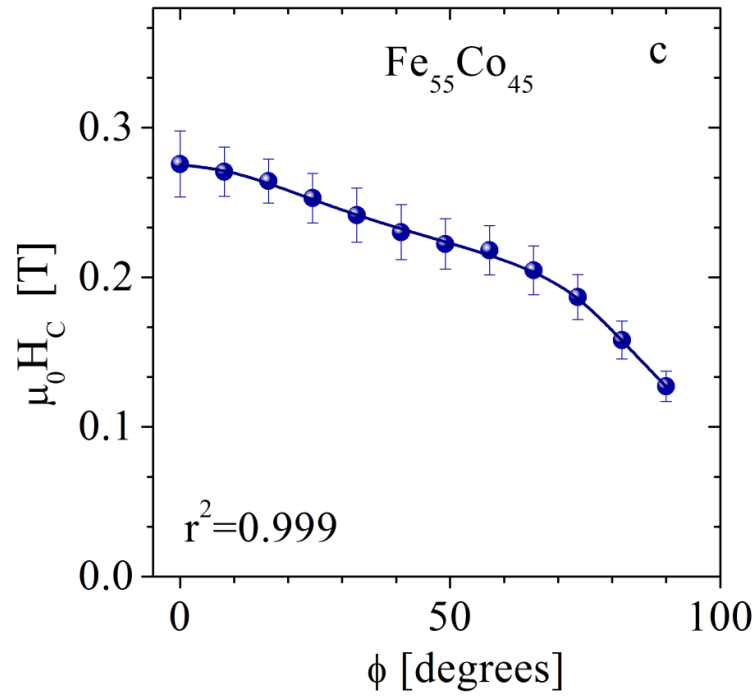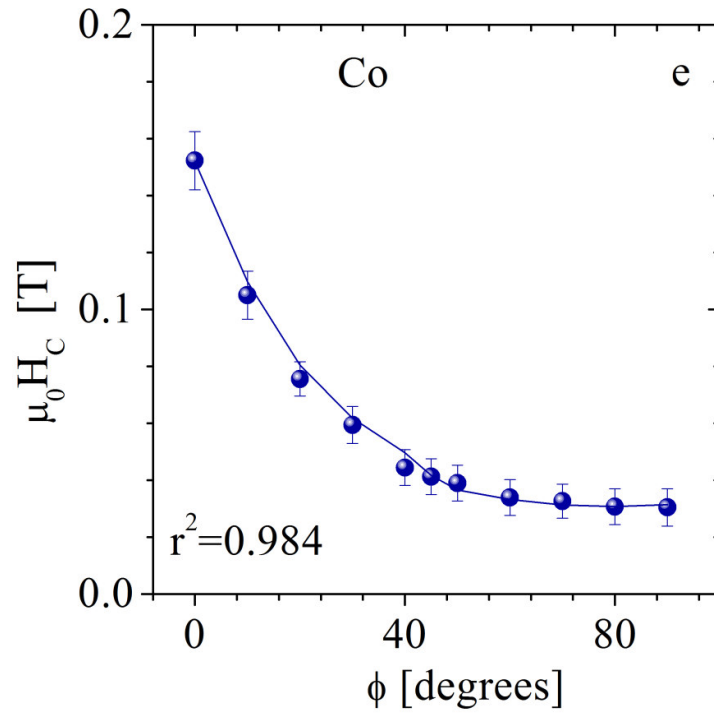
Figure 6. Angular dependence of the coercive field for the nanowire arrays investigated; ϕ is the angle between the applied magnetic field and the long wire axis. Symbols denote the experimental data and, depending on the wire nanostructure and composition, the solid lines correspond to predictions of eqns. (3) and/or (5).

****